Magnetic Nanoparticle Decorated Anodic Alumina Nanotubes for Fluorescent Detection of Cathepsin B

J.T. Domagalski, E. Xifre-Perez, M.A. Tabrizi, J. Ferre-Borrull, L.F. Marsal*

Departament d'Enginyeria Electrònica, Elèctrica i Automàtica, Universitat Rovira i Virgili, Avinguda dels Països Catalans, 26, 43007, Tarragona, Spain; jakub.domagalski@urv.cat; elisabet.xifre@urv.cat; mahmoud.amouzadeh@urv.cat; josep.ferre@urv.cat

* Corresponding author at: Departament d'Enginyeria Electrònica, Elèctrica i Automàtica, Universitat Rovira i Virgili, Avinguda dels Països Catalans, 26, 43007, Tarragona, Spain; lluis.marsal@urv.cat +34 977559625

Abstract

In this work, we present the process to provide anodic alumina nanotubes with magnetic responsivity based on magnetic nanoparticles. We demonstrate the possibility to cause the motion of these composite nanotubes under magnetic field, providing them with guided mobility. The obtained magnetic anodic alumina nanotubes are completely characterized and their potential to undergo selective and effective functionalization, and stimuli-responsive load release is demonstrated. For this purpose, protease-triggered release of fluorescent molecules loaded inside the magnetic anodic alumina nanotubes (MAANTs) by selective functionalization is performed. The inner walls of the MAANTs were selectively covered with protein padding of albumin-fluorescein isothiocyanate conjugate (FITC-BSA) through means of silanization. Protein functionalization was designed to undergo proteolytic hydrolysis in presence of cathepsin B- protease highly expressed during growth and initial stages of tumor metastasis – in order to cleave peptide bond of albumin and release fluorescent fragments of the protein. Proteolytic reaction with the enzyme is performed under acidic conditions. Presented arrangement is an exemplary combination of functionalities – which are vast – and of value for applications like drug delivery and biosensing applications.

Keywords: Anodic Alumina Nanotubes, Magnetic Properties, Stimuli-Responsive Release, Cathepsin B, Self-Assembly

MAANTs: magnetic anodic alumina nanotubes; **FITC-BSA:** albumin-fluorescein isothiocyanate conjugate; **CNTs:** carbon nanotubes; **PAA:** porous anodic alumina; **AANTs:** anodic alumina nanotubes; **PBS:** phosphate buffered saline; **DI:** deionized; **ESEM:** environmental scanning electron microscope; **ETD:** Everhart-Thornley detector; **BSE:** backscattered electron; **EDX:** energy dispersive X-ray; **FTIR:** Fourier-transform infrared spectroscopy; **ATR:** attenuated total reflectance; **DLS: dynamic light scattering**; ***J*:** current density [mA/cm^2]; **GA:** glutaraldehyde; **APTES:** (3-aminopropyl)triethoxysilane

1. Introduction

Development of new materials and constant progress of technology enable to produce more advanced and highly specified systems based on nanoparticles. Due to scale, nanostructures can interact with biological systems in ways not possible before, they exhibit unique interaction with electromagnetic radiation and have intrinsic properties originated from unprecedented surface area to volume ratio. Quantum dots, nanospheres, nanorods, nanostars, nanotubes and many more, composed from different chemicals and in a range of sizes have been developed [1]–[5]. Amongst the most popular – with almost 200,000 results with Elsevier search engine – high aspect ratio hollow inside elongated structures called nanotubes, carbon nanotubes being (CNTs) the most prevalent example [6].

Means to functionalize nanotubes and their potential applications are vast [7]–[11]. An important aspect of nanosized particles behavior is their motion – both passive and active – especially for the interaction with biological systems where precision and selectivity is crucial [12]–[14]. Passive solutions can conveniently exploit properties of the environment, although they lack rapid and precisely aimed movement. Attachment of magnetic nanoparticles to bigger nanostructures – either covalently or electrostatically – is common practice to provide these nanostructures with magnetic properties [15]. For example, nanotubes with enhanced maneuverability can serve as nanoadsorbent for selective removal of heavy metal ions and organic molecules as they enable impurities removal by simply using a magnet [16], [17]. Magnetic responsivity of carbon nanotubes decorated with magnetic nanoparticles enabled to form epoxy laminate preserving forced orientation of nanotubes, providing superior mechanical properties and reduced thermal expansion of the composite [18]. Nanotubes modified with magnetic nanoparticles serve as electromagnetic attenuation material in electronic components [19]. What is more, bigger nanoparticles coated with small magnetic nanoparticles can display three dimensional magnetism – newly emerging approach to nanomagnetism. For bioimaging, magnetic and fluorescent carbon nanotubes have been demonstrated to work effectively as imaging agents for the observation on living mice [3]. Physical effects featuring geometry, topology and chirality provide their potential use in memory and sensing [20]. In future, it may be possible to create nanoparticle motors/robots with precise movement control [21]. In general, systems based on nanoparticles have potential to bring novelty in many fields. Apart from broadly known materials with long history, new materials are being developed as well.

Porous anodic alumina (PAA) is a material generated through environmentally friendly and facile process of electrochemical aluminum etching in acid electrolyte. With tailored parameters of the anodization process, highly ordered hexagonal array of perpendicularly aligned pores of aluminum oxide can be formed on the surface of aluminum anode [22]–[25]. In addition, under specific anodization conditions, the pore diameter can be modulated in depth or combine different pore diameters in the same structure [26]–[28]. Moreover, process carried out under high current density may yield structure with weaker connection between adjacent pores – sometimes featuring voids at three cell junction or loose array of pores [29]. This "cell separation phenomenon", combined with pulse pattern of high-low current input leads to formation of highly regular modulated structure that – after specific treatment – can be split into well-defined nanoparticles called anodic alumina nanotubes (AANTs) [30], [31]. As prepared nanotubes have no catalyst contamination and low surface reactivity. Their surface is rich in hydroxyl group, an important factor that determines the surface charge of the nanotubes and enables to provide covalent/electrostatic modification. Zeta potential of AANTs in acidic PBS is positive, becomes neutral at pH 4.3 and remains negative in higher pH [32]. Specificity of the synthesis allows easy regulation of the resulting nanotube length with a slight adjustment of the process parameters. These features make AANTs attractive candidates as model nanostructures for toxicity studies. Their interaction with cells has been analyzed by Wang and colleagues. It has been demonstrated, that alumina nanotubes exhibit superior biocompatibility – during 3 days exposition to 700 nm average length nanotubes cell viability of RAW 264.7 and MDA-MB231-TXSA cell lines was consistently above 90%. This behavior is, however, length dependent as increasing nanotoxicity has been reported for longer nanotubes (>2.5μm) [32], [33]. Another advantage lays in the nature of the fabrication process that allows the selective functionalization of the inner surface of the nanotube independently of the outer surface. Additional procedures for selective surface modification or purification/shielding steps are not needed enabling precise design of the multifunctional nanoparticle system. The first study reporting such possibility was carried out solely by incubation of the PAA in drug solution, prior to the separation of the structure [33].

In this paper, we present the development of magnetic anodic alumina nanotubes, their design and functionalization for enzyme-triggered release of the nanotubes' load. To our knowledge, this is the first work to report anodic alumina nanotubes provided with magnetic responsivity. A complete characterization of the MAANTs is presented. Besides, the MAANTs are designed and optimized for enzyme-triggered release of fluorescent protein fragment. Protein

padding of albumin fluorescein isothiocyanate conjugate was created solely inside the nanotubes exploiting top-down fabrication approach and initial integrity of the porous structure. Functionalization steps were followed with microscopic and spectroscopic analysis of the sample. Performance of these magnetic nanotubes is demonstrated using cathepsin B – protease highly expressed during cancer growth and early stages of metastasis. The developed MAANTs have a high maneuverability in response to magnetic fields. This very interesting property along with the high degree of structure's regularity makes MAANTs valuable nanostructures in many fields like drug delivery, detection and precise separation.

2. Materials and methods

2.1. Materials

Aluminum (Al) discs of thickness 0.5 mm and purity 99.999 % were supplied by Goodfellow Cambridge Ltd. Sulfuric acid (H_2SO_4, 95.0-98.0 % ACS reagent), ethanol absolute (C_2H_5OH, 99.9 % ACS reagent) and hydrogen peroxide (H_2O_2, 30 %, stabilized) were purchased from Scharlau. Cooper (II) chloride dihydrate ($CuCl_2$, ≥ 99.0 % ACS reagent), hydrochloric acid (HCl, 37% ACS reagent), perchloric acid ($HClO_4$, 70.0-72.0 % ACS reagent) and glutaraldehyde 25 wt. % in H_2O (GA) were purchased from Sigma-Aldrich. (3-aminopropyl)triethoxysilane (3-APTES, 99 %) was purchased from Aldrich. Albumin-fluorescein isothiocyanate conjugate from bovine (FITC-BSA), phosphate buffered saline (PBS, BioPerformance, pH 7.4) and cathepsin B from bovine spleen lyophilized powder, ≥ 10 units/mg protein were bought from Sigma. Aforementioned chemicals were used as received. Iron oxide nanoparticles (II, III) 10 nm avg part. size (TEM) carboxylic acid (citrate) functionalized 5 mg/mL in H_2O dispersion were supplied by Aldrich and followed purification protocol of resuspension cycles and finally suspended in 0.01 M PBS pH = 7.4. Deionized (DI) H_2O PURELAB® Option-Q (18.2 MΩcm) was used for preparing all the solutions used in this study.

2.2. Characterization methods

Electron microscope images and elemental composition of the materials were measured with environmental scanning electron microscopy (ESEM, FEI Quanta 600) using Everhart-Thornley detector (ETD) and backscattered electron (BSE) detectors and energy dispersive X-

ray (EDX) function, number of iterations for EDX measurement was 4. Structured films were coated with a ~5 nm thin layer of gold prior to ESEM imaging. Before EDX analysis, a suspension of nanotubes was deposited on copper tape and dried. Structure was characterized with Fourier-Transform Infrared Spectroscopy with ATR attachment (Fourier Jasco FT/IR-600 Plus with ATR S) to verify successful covalent conjugation with protein, with a measurement resolution of 0.96 cm^{-1}, accumulation of 32 with applied incident angle of 45°. ζ-potential and dynamic light scattering (DLS) were measured with a ZetaSizer Nano, using 0.6 mg/mL suspension of nanotubes and 12.5 μg/mL maghemite colloid at 25°C. All samples were cold-sonicated for 10 s prior to measurement. Each result of ζ-potential was an average of 3 individual measures that consisted of at least 12 runs each, while hydrodynamic diameter measurement consisted of 12 runs processed by Malvern® software. AANTs and MAANTs geometric features and morphology were captured with transmission electron microscopy (TEM, JEOL model 1011). Size distribution of the AANTs was prepared based on 300 individual measurements for each nanotubes dimension from TEM images analyzed with ImageJ software. Proteolytic hydrolysis of the albumin and resulting release of the fluorescent component caused by cathepsin B has been followed by measuring fluorescence emission intensity with spectrophotometer (Photon Technology International Inc, Birmingham, NJ) with Xe lamp light source. All measurements were performed at room temperature with excitation wavelength of 450 nm, emission spectrum was measured between 340 and 600 nm with a resolution of 1 nm. Finally, fluorescence images were acquired using a Nikon Eclipse TE2000-E inverted microscope mounted with a C1 laser confocal system (EZ-C1 software, Nikon). Excitation source applied was 488 nm argon laser and the emission was collected at 515 ± 15 nm using a bandpass emission filter (green channel). All confocal images were captured using a 5 MP CCD, objective x100 and excitation time of 500 ms. A xs analytical balance with 0.01 mg readability (KERN ABT 120-5DNM) was used during all experiments for sample weighting. Sonication was performed using a sonicating bath Bandelin Sonorex RK 102H.

3. Magnetic anodic alumina nanotubes (MAANTs)

3.1. Preparation of magnetic anodic alumina nanotubes

Aluminum discs were sequentially sonicated in ethanol and ultrapure water for 10 min each. Prior to anodization, Al discs were electropolished in a mixture of $HClO_4$ and ethanol 1:4

(v/v) under 20 V at 5°C during 7 min. Then, the first anodization step was performed in an aqueous 0.3 M H_2SO_4 electrolyte modified with 10% ethanol at 25 V and 8°C for 20 h to generate a starting nanoporous anodic alumina layer of ~110 µm. Next, the anodization process was switched to galvanostatic pulse anodization, using the same acid electrolyte but at 1°C under vigorous stirring. Pulse anodization consisted of sequential pulses between mild anodization and hard anodization regimes, in which the current density (*J*) input was periodically switched between low and high values for a given time in a stepwise fashion. Each pulse was formed by a mild anodization step at 4.5 mA/cm^2 for 5 s and hard anodization step at 390 mA/cm^2 for 3.5 s. The formation of nanostructured PAA and the course of pulse anodization are visualized in **figure 1A**. The obtained structured PAA film was chemically etched to remove aluminum support and weaken the structure to provide good separation into nanoparticles. Impact on the morphology of PAA film during acid etching has been reported previously – cell boundaries in horizontal and vertical axes has been significantly exposed [31].

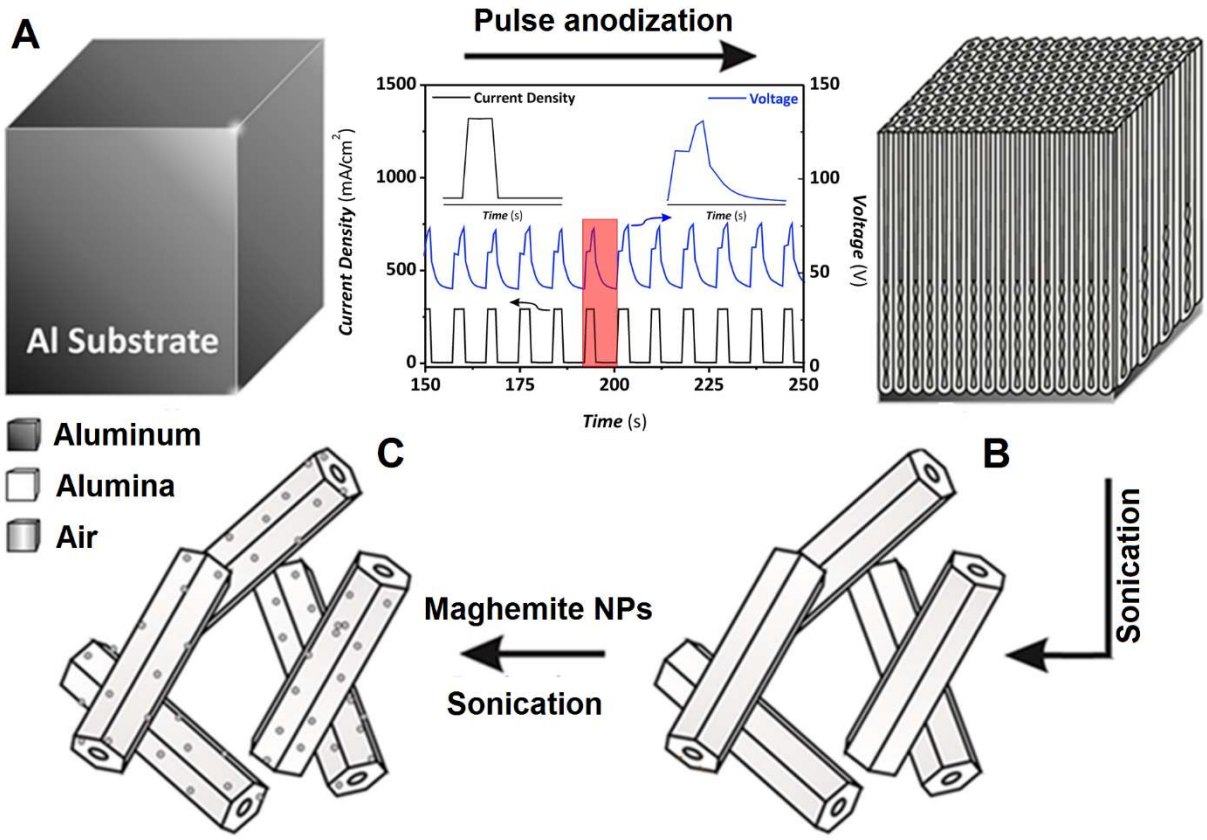

Figure 1. Fabrication of magnetic alumina nanotubes. (A) pulse anodization of aluminum resulting in formation of a periodical porous structure; (B) liberation of nanotubes and (C) interaction of the nanotubes with maghemite nanoparticles.

Ice bath sonication for 20 minutes was performed on etched PAA film immersed in DI water pH = 7.0 to yield highly regular nanotubes (**fig. 1B**). It has been observed that sonication in PBS produces a visible degradation after 20 minutes, similarly to the degradation attributed to an increment of temperature observed in previous works [44]. For this reason sonication in PBS is carried out only in 10 s periods. Nanotubes and maghemite nanoparticles are centrifuged and dispersed in 0.01 M PBS pH = 7.4, 5 % hydrochloric acid solution was utilized to reach expected pH. PBS pH = 7.4 provides better stability of the suspension than DI H_2O, reduces aggregation effects over time and is utilized for long storage of as-prepared AANTs. Since surface of alumina nanotubes is charged in aqueous suspensions, it is possible to initiate electrostatic interaction with particles exhibiting opposite surface charge. Initial experiments allowed to estimate the ratio of nanoparticles to nanotubes at which saturation occurs (unbounded maghemite nanoparticles detected by DLS). This facile approach enabled to provide nanotubes with magnetically induced motion. The positively charged nanotubes were mixed with excess of carboxylic acid functionalized maghemite nanoparticles, stirred overnight and centrifuged several times to remove unbounded maghemite nanoparticles, obtaining MAANTs (**fig. 1C**).

3.2. Characterization of magnetic anodic alumina nanotubes (MAANTs)

Cross-section of the structured PAA film formed with pulsed chemical anodization is presented in **fig. 2A**. The structure displays the characteristic pore diameter modulation caused by current pulse oscillations. After sonication and functionalization with magnetic nanoparticles, the resulting MAANTs were deposited on copper tape and observed under ESEM (**fig. 2B**). The magnetic nanoparticles are difficult to observe using standard ETD detector due to their small size (10 nm). Their presence becomes more apparent when back-scattering detector is applied (**fig. 2C**). Since backscattering effect is stronger with elements of higher atomic number, areas with different chemical composition can be clearly distinguished.

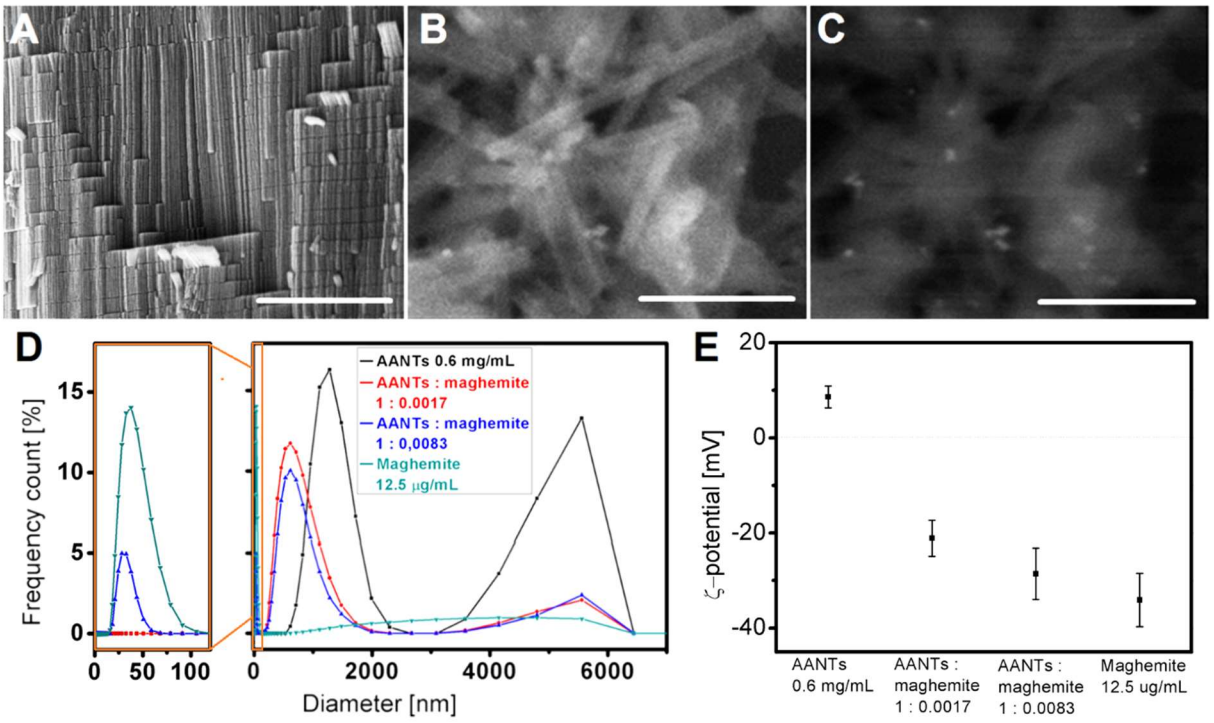

Figure 2. (A) ESEM cross-section of structured PAA; (B) ESEM image of MAANTs and (C) BS ESEM image of MAANTs; (D) DLS size distribution of AANTs, maghemite nanoparticles and AANTs mixed with maghemite in 0.01 M PBS pH = 3.6 and (E) ζ-potential measurements of AANTs and AANTs mixed with different ratios of maghemite nanoparticles in 0.01 M PBS pH = 3.6. Scale bars: 5 µm, 1 µm and 1 µm respectively.

AANTs are composed of amorphous alumina. The surface of this material features a high density of oxygen groups. As a result of protonation in H_2O, these groups are responsible for positively charged surface in a broad range of pH. When mixed with negatively charged maghemite NPs – self-assembly driven by electrostatic force occurs. On the other hand, AANTs in PBS are negatively charged for pH 5-8, reaching isoelectric point at pH = 4.3. Below this value, AANTs are positively charged [33]. To evaluate effects of interaction between nanotubes and maghemite nanoparticles and estimate concentration of maghemite colloids needed for effective interaction with nanotubes, unmodified nanotubes were combined with several different concentrations of magnetic nanoparticles: 1, 2, 5, 10, 25, 50 and 100 µm/mL in 0.01 M PBS pH = 3.6. Nanoparticle colloids and nanotube suspension were mixed and stirred overnight. DLS measurements as well as the collection of samples for TEM were preceded by 10 s of cold sonication. For the lowest concentration, the presence of maghemite nanoparticles was barely visible. However, for the highest concentration, coating of the maghemite nanoparticles is formed. Two different concentrations – before and after saturation – were selected: 10 and 50 µg/mL. Their hydrodynamic diameter and ζ-potential

were measured, including those of as-prepared AANTs and maghemite nanoparticles for comparison (**fig. 2D-E**). Accuracy of DLS size measurement is the highest for spherical nanoparticles. For that reason, determination of size of high-aspect ratio materials like nanotubes wields level of uncertainty. These results, however, can still be informative with regards to behavior of colloid dispersion and tendency to form clusters [35]. Size distribution of unmodified AANTs display two major peaks: one at 1290 nm representing singular nanotubes along with small clusters and another at 5560 nm representing bigger agglomerates. It is clear, that addition of maghemite nanoparticles results in a shift towards smaller size indicating increase of repulsive forces and higher stability of the suspension [36]. We expect that presence of carboxylic groups on magnetic nanoparticles provide for more pronounced electrostatic character. Apart from higher prevalence of smaller particles, signal representing bigger agglomerates decreased significantly. What is more, the addition of a higher quantity of magnetic nanoparticles (8.3 μg for 1 mg of AANTs) leads to saturation – excess of maghemite nanoparticles represented by peak at 38 nm.

These observations are supported by ζ-potential measurements shown in **fig. 2E**. At given conditions, unmodified suspension of 0.6 mg/mL nanotubes display positive potential value of 8.6 ± 2.3 mV, while 12.5 μg/mL maghemite nanoparticles have negative ζ-potential of -34.1 ± 5.61 mV. The charge difference between positively charged nanotubes and negatively charged maghemite (reflected in measured ζ-potential) enabled to achieve self-assembly with no presence of surfactants [37]. When nanotubes and nanoparticles are mixed at different weight ratios of 1:0.0017 and 1:0.0083, measured ζ-potential is -21.1 ± 3.82 mV and -28.6 ± 5.42 mV respectively. It is expected that this increase of absolute charge is reflected in the DLS size distribution, since repulsive forces reduce nanotubes' tendency to aggregate.

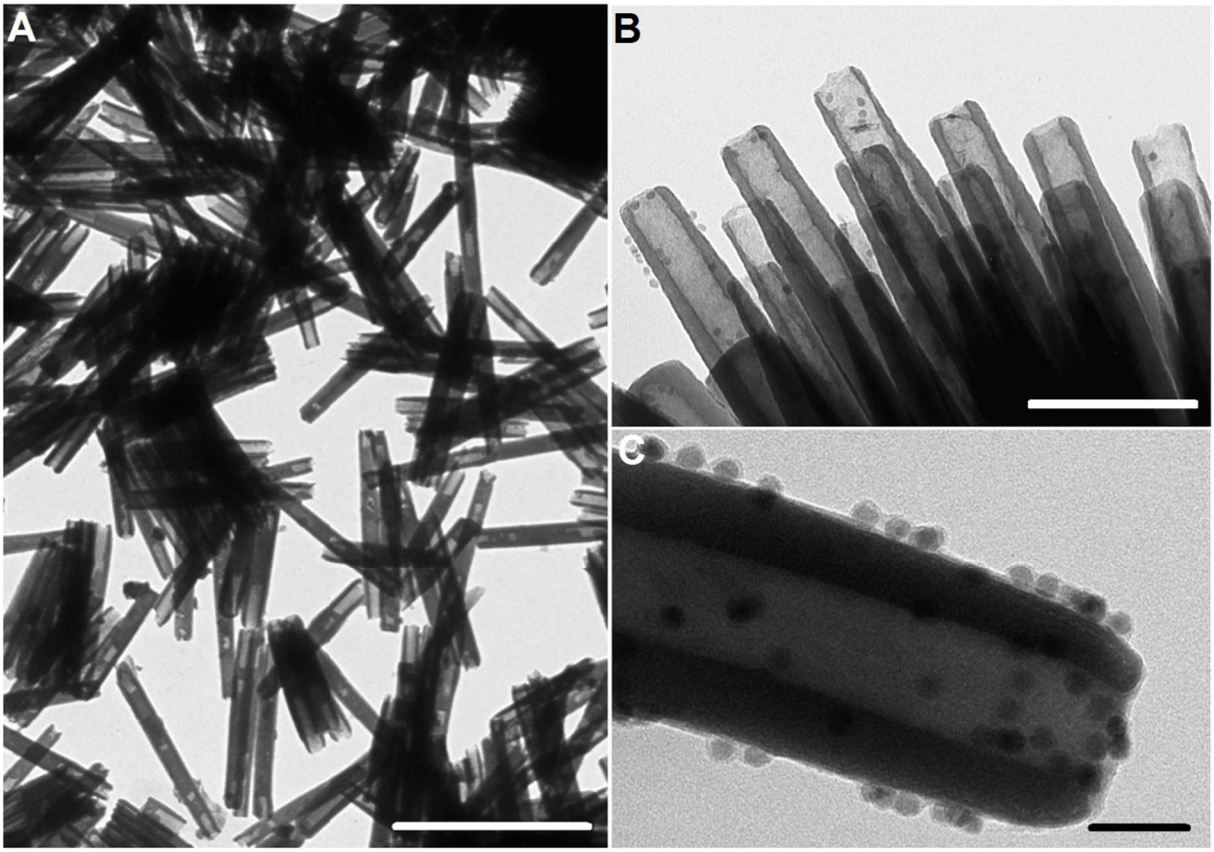

Fig. 3. (A) TEM overview on unmodified AANTs; (B) TEM image of MAANTs and (C) magnified view of individual MAANT; Scale bars: 1μm, 200 nm and 50 nm respectively.

The individual nanotubes can be easily distinguished. Liberated AANTs are shown in **fig. 3A.** These nanotubes are later combined with excess of maghemite nanoparticles. Basing on TEM images, calculated average length of created structures was 1008 ± 118 nm. Additionally, average outer diameter of the tube was 65.5 ± 10.1 nm while average inner diameter is 36.8 ± 5.7 nm. **Fig. 3B-C** reveals successful attachment of superparamagnetic nanoparticles that can be observed as small spheres on the surface of these nanotubes (average diameter of maghemite nanoparticles is 10 nm). These nanotubes are magnetic field-responsive and their motion can be easily observed (see Video S1 in the **Supporting Information**).

4. Stimuli-responsive release of MAANTs load for drug delivery and biosensing applications

Our work aims to lay foundation towards employing this novel material in more advanced multifunctional systems. These biologically inert nanotubes can be designed to serve in many

fields like drug delivery, biosensing and catalysis [38]–[40]. In this section, we describe in detail how nanotubes with magnetically induced mobility can be successfully used as reservoirs with stimuli-responsive release of their load. Concretely, the triggered release of fluorescent protein fragments due to the interaction of the protein layer with proteolytic enzyme cathepsin B is proved. Description of the synthesis is followed by explanation of the experimental setup in which magnetic mobility and enzymatic responsivity is demonstrated.

4.1. Magnetic AANTs(FITC-BSA) fabrication and characterization

For this experiment, a selective functionalization of the inner wall of the nanotubes has been performed. For this purpose, the MAANTs formation steps presented in **Fig.1** have been combined with the functionalization procedure. To provide protein cladding exclusively on the inner part of the nanotubes, silanization process is performed before dividing PAA structure into nanotubes as outer walls of the structure are inaccessible at this stage. Chemical changes that occurred during functionalization with protein are presented in **Fig. 4.** The PAA substrate with ordered and structured pores **(Fig. 4A)** was immersed in 0.3 M H_2O_2 at 70°C for 1 h in order to activate hydroxyl groups on the surface of the aluminum oxide (**fig 4B**). Then, sample was cleaned and dried in oven for 3 hours at 110°C. Afterwards, introduction of silane groups was performed through immersion of sample in 3:1 mixture of ethanol and H_2O v/v with 1% of APTES. Solution is heated to 45°C. The addition of water initiates the reaction (**fig. 4C**). After reacting for 2 h, the sample is washed and dried in oven at 110°C overnight. After reaction with APTES, the remaining Al substrate was removed by wet chemical etching in a mixture of 0.2 M $CuCl_2$ and 6.1 M HCl followed by further immersion of the structured nanoporous anodic alumina film into the same etchant solution for 1 h. The structured PAA film is then dried and weighted – difference in mass of the template before and after liberation of the nanotubes was used to calculate initial concentration of the suspension. Suspension was later diluted to reach final concentration. Nanotubes template was immersed in DI H_2O and sonicated for 15 minutes in ice bath (~5°C) to liberate the nanotubes (**fig. 4D**). Incorporation of crosslink and albumin is performed after sonication in order to avoid potential damage to the protein. Glutaraldehyde (GA) is added to the suspension with final concentration of 2.5 % and shaken for an hour (**fig. 4E**). Attachment of crosslink is followed by addition of albumin-fluorescein isothiocyanate conjugate (5 %) and subjected to overnight stirring (**fig. 4F**). Sample is centrifuged several times to remove excess reagent. Several cycles of centrifuging and redispersion in water were applied.

After thorough washing, water was changed for PBS pH = 4.1 needed for enzymatic reaction and electrostatic interaction. Change of pH was necessary for enzymatic cleavage experiment. Both AANTs and albumin become positively charged in acidic pH (positive charge is further increased when FITC-BSA is attached). Yet, activity of cathepsin B decreases with increasing acidity. Reported pH of 4.1 was the highest at which electrostatic interaction between AANTs(FITC-BSA) and maghemite nanoparticles could occur. Finally, AANTs(FITC-BSA) become magnetic by mixing 0.6 mg/mL AANTs(FITC-BSA) suspension with 12.5 μg/mL maghemite nanoparticles colloid and shaken intensively overnight. Suspension was repeatedly cleaned to remove excess of magnetic nanoparticles (**fig. 4G**). Hydrodynamic diameter and ζ-potential measurements were carried out on the same day as MAANTs(FITC-BSA) preparation.

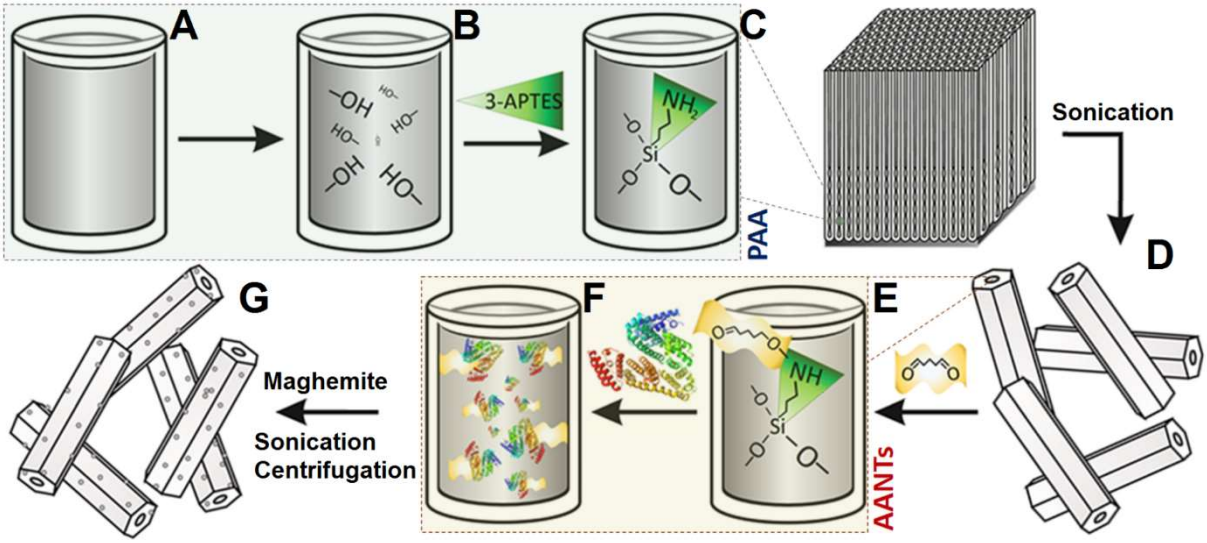

Figure 4. Schematics of MAANTs(FITC-BSA) fabrication and enzymatic triggered release: (A) PAA structured film with unmodified pores; (B) activation of hydroxide groups; (C) attachment of APTES; (D) liberation of nanotubes through sonication; (E) addition of GA crosslink; (F) functionalization with protein and (G) electrostatic decoration of AANTs with maghemite nanoparticles.

Verification of successful formation of chemical bonds during the functionalization of the MAANTs was carried out with FTIR. First measurement was performed prior to silanization on as prepared PAA. After silanization and attachment of the albumin, PAA(FITC-BSA) was measured to compare occurring changes. Results of analysis shown in **figure 5A** are consistent with previous reports [41], [42]. Modification was confirmed by appearance of peaks of Si-Al-O at 1105.98 cm^{-1}, -NH bending at 1643.05 cm^{-1}, C=O stretching at 1729.83

cm^{-1}, CH_3 stretching at 2850.27 cm^{-1} and CH_3 stretching at 2917.77 cm^{-1} indicating successful creation of silane bond and attachment of the albumin.

Functionalization of nanotubes and self-assembly of maghemite-AANTs composite were observed at different stages with measurements of ζ-potential (**figure 5B)**. Unmodified nanotubes in acidic PBS (pH = 4.1) exhibit positive ζ-potential of 2.08 ± 0.69 mV. When inner wall of the tube is modified with albumin, ζ-potential value increases and reaches 4.01 ± 0.77 mV. We expect this increment of charge being related to the appearance of positively charged protein [43]. After intense mixing and a few washing steps, obtained composite shows negative ζ-potential of -4.77 ± 0.74 mV.

Elemental composition of MAANTs(FITC-BSA) is shown in **figure 5C**. In principle, nanoporous anodic alumina consists of aluminum and oxygen, with traces of the electrolyte present in the structure, the amount of which depends on the process conditions [44]. Our recent study provides some insight into elemental composition of PAA fabricated under hard anodization pulses [45]: considerable increase of sulfur content is observed compared to alumina obtained under more commonly anodization conditions [46]. Apart from significant share of sulfur in the structure, phosphorus from PBS buffer can be observed along with carbon and trace quantity of iron, that are expected to indicate presence of protein and iron oxide nanoparticles respectively.

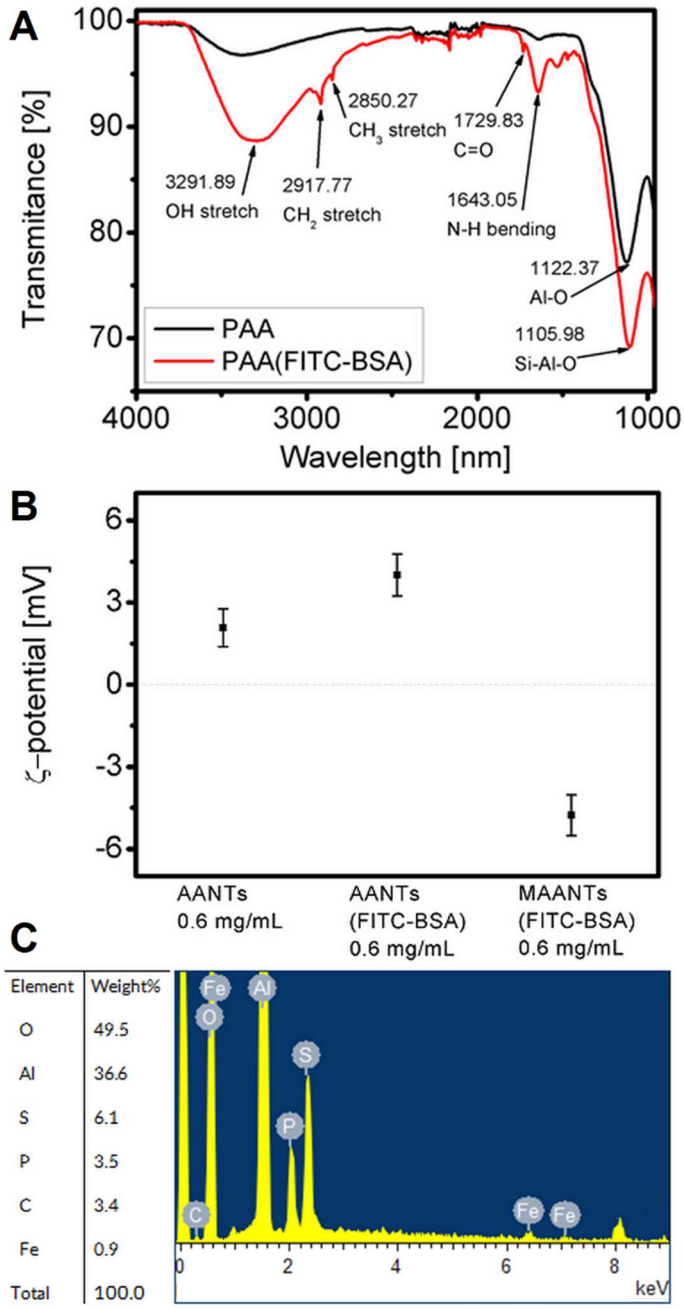

Figure 5. Characterization of PAA template and nanotube colloid (A) FTIR-ATR characterization of PAA; (B) ζ-potential measurements of nanotubes after consecutive functionalization steps (0.01 M PBS pH=4.1) and (C) elemental distribution of MAANTs(FITC-BSA).

4.2. Interaction of MAANTs(FITC-BSA) with cathepsin B

Proteases are class of enzymes that catalyses proteolysis – breakdown of proteins into polypeptides and amino acids through peptide bond cleavage. While exopeptidases cut single

amino acids of the terminal peptide bond – endopeptidases such as cathepsin B – flank specific scissible peptide bond. Cleavage site is based on the recognition of the specific amino acid sequence in the protein by enzyme's subsite (**Figure 6**). In general, cathepsins are not very specific enzymes. S2 site is the only defined pocket and along with S1 and S1' comprise major recognition sites of cathepsins. They exhibit pronounced preference for small hydrophobic amino acid residues in the P2 position (Leu, Val, Ile). Exception for cathepsin B is also acceptance of Arg in P2 position [47]. Analyzing sequences of bovine serum albumin derived peptides, it has been revealed that cleavage occurs between following residues: Arg^{81}-Glu^{82}, Val^{223}-Glu^{424} and Gly^{430}-Lys^{431}. Cathepsin B cleaves BSA into several relatively large fragments [48]. Interaction between enzyme and FITC-BSA leads to release of these FITC-labeled protein residues into the solution.

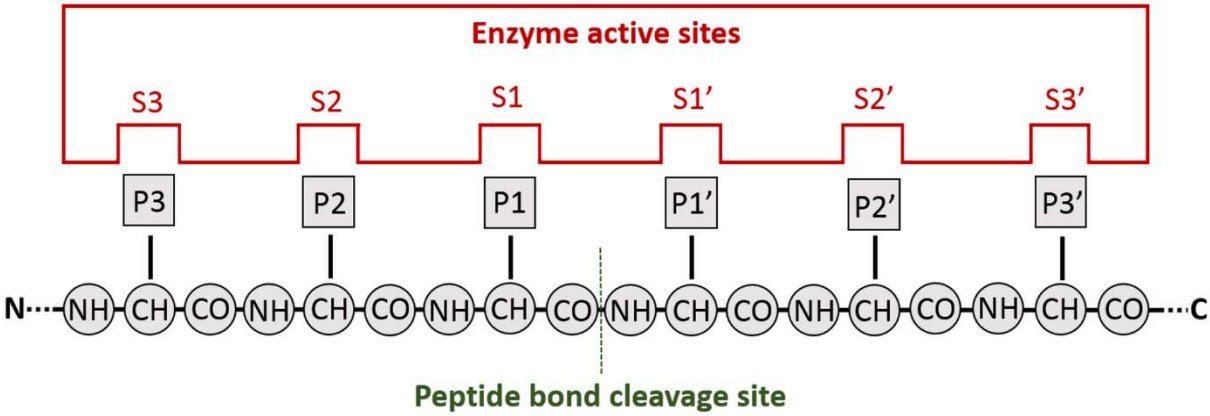

Figure 6. Proteolytic interaction between protease and polypeptide using Schechter and Berger nomenclature for substrate-protease interactions. Active site of a protease contain several subsites. Subsites are marked in both directions from the catalytic site (green line). Sites S1-S3/S1'-S2' of the enzyme corresponds to P1-P3/P1'-P3' locations of amino acid residues in the peptide substrate. Cleavage takes place between P1 and P1' residues.

All MAANTs(FITC-BSA) experiments were performed 48 h after FITC-BSA incubation (24 h after maghemite nanoparticles attachment). To prevent damage to the chromophore, samples were stored in cool place without light. Cathepsin B at concentration of 8.3 ng/mL (220 nM) has been introduced into 0.6 mg/mL MAANTs(FITC-BSA) suspension. Injection was followed by intense stirring. Then, precipitation of nanotubes was accelerated with a magnet. To measure fluorescence, particles were separated from the main volume of the liquid to prevent contribution of protein fragments inside MAANTs(FITC-BSA).

Magnet and sample were hold in racks preserving their location during the experiment. Sample was kept above the magnet for 15 minutes, and then analyte solution was measured with spectrophotometer, reintroduced to the suspension and shaken again. These steps were repeated at time intervals of 15, 30, 60, 90 minutes and 2, 4 hours. Schematic arrangement of the experiment setup is shown in **figure 7A-C**. To promote homogenous distribution of the fluorescent protein fragments in measured sample, it was shaken intensively every time prior to precipitation using magnet. Movements of the magnetic suspensions can be observed with naked eye. Such maneuverability in response to the magnetic field together along with the high regularity of the structure makes them a valuable material in many fields like drug delivery, detection and precise separation procedures.

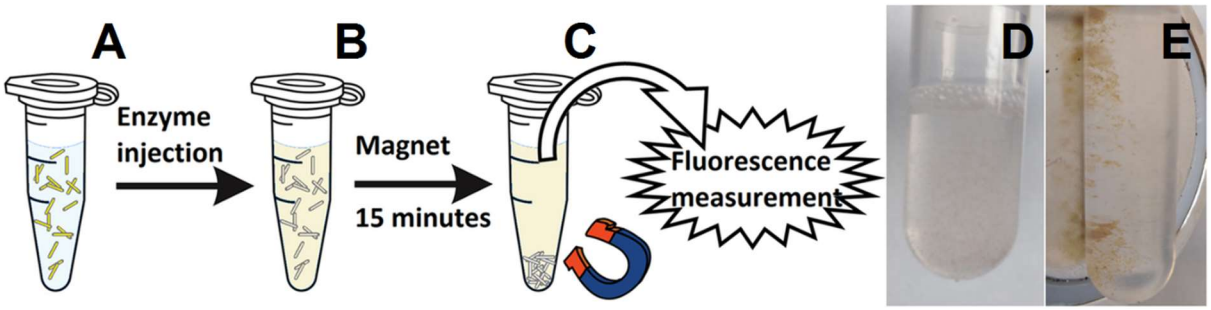

Figure 7. Visualization of proteolysis-based release of fluorescent component and manipulation of the sample with magnetic field. (A) represents nanotubes with load inside; (B) release of fluorophore into solution; (C) accelerated precipitation of nanotubes precipitate after release; (D) image of dispersed MAANTs(FITC-BSA) suspension and (E) attracted to the wall of the vial with N52 magnet.

Images of experimental setup for interaction experiment are shown in **figure 7D-E**, with MAANTs(FITC-BSA) in suspended form and precipitation with N52 magnet. After injection of the cathepsin B, the release of fluorescent protein fragments was followed with a spectrophotometer (**fig. 8A**). Initial sudden surge slowed down and reached steady state 4 hours after succeeding the injection of the enzyme. Although cathepsin B is considered moderately active enzyme, majority of reports finish kinetics curve measurement after 1 h. Taking into account high concentration of enzyme applied (220 nM) we suspect other effects like diffusion and steric hindrance to slow down observed release [49], [50].

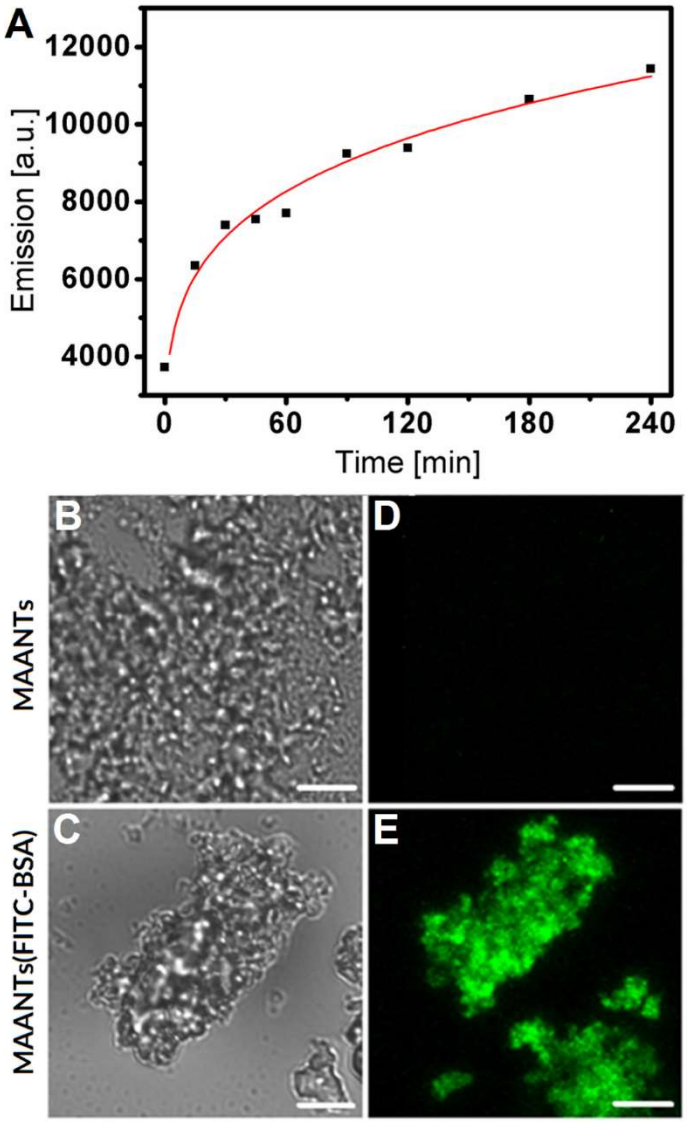

Figure 8. Experimental setup and measurements of fluorescent emission. (A) PL spectrum of fluorescent release driven by cathepsin B proteolysis of FITC-BSA and (B-C) white light and (D-E) confocal microscope images of MAANTs and MAANTs(FITC-BSA). Scale bar 10 µm.

Nanotubes itself are too small to be structurally distinguished using confocal microscopy due to physical limitation of the method. **Figure 8B-C** presents images acquired with optical microscope that represent cluster of nanotubes. Nanotubes without FITC-BSA functionalization do not exhibit any fluorescent emission at given conditions. Magnetic AANTs(FITC-BSA) (**fig. 8D-E**), however, show intense emission in the green light region (515 – 530 nm detector) originated by the fluorescein presence [50].

5. Conclusions

Previous approaches enabled to establish technology that provides highly regular anodic alumina nanotubes through process of aluminum electrochemical etching [31], [45]. Low nanotoxicity of as-prepared material and high loading capacity has been demonstrated through interaction with biological systems – several cell lines and rodent species –laying foundation for future applications as a biomaterial and for drug delivery [32], [33], [51]. In this study we present the first work to our knowledge reporting anodic alumina nanotubes provided with magnetic responsivity and displaying potential to undergo selective, effective functionalization and stimuli-responsive release of their load. Successful self-assembly of maghemite nanoparticles-nanotube composite based on opposite surface charge was followed with ζ-potential measurements and observed under TEM. Moreover, it was possible to transfer the mobility of magnetic nanoparticles guided under magnetic field to the alumina nanotubes causing directional motion of the composite nanotubes. Proper design of magnetic high-aspect ratio material enables to combine manuvereability and controlled release – valuable for drug delivery – as demonstrated by Fizir et al [52]. In our report, magnetic responsivity has been employed to ease course of proteolysis experiment. Functionalization and successful attachment of albumin protein was demonstrated with FTIR with appearance of bond-specific signal attributed to formation of specific covalent bonds. Protein functionalization has been carried out utilizing similar approach to previously presented by Tabrizi et al. for aptasensors fabrication previously [53]. In this work PAA formed through pulse anodization is employed, which enables to yield selective inner-wall functionalization prior to dividing structure into nanotubes. Effectivity of the system to respond with the presence of cathepsin B was demonstrated with photoemission experiment. Initially, the concentration of released fluorescent compound increases rapidly reflecting the quick response to the presence of the enzyme, and stabilizes after 4 hours. This study demonstrates the great potential of the MAANTs for developing magnetically guided sensors aimed at the detection of biomolecules or drug release vehicles for localized treatments. Taking into account novelty of magnetic nanoporous anodic alumina nanotubes, our finding provide alternative to commonly used nanoprobe systems. Further efforts to optimize the process, aiming at enhanced colloidal stability and robustness of the structure, are under way so that MAANTs can become more accessible in various environmental conditions.

Declaration of competing interest

The authors declare that they have no known competing financial interests or personal relationships that could have appeared to influence the work reported in this paper.

CRediT authorship contribution statement

J.T. Domagalski: Writing - original draft, Conceptualization, Methodology, Investigation, Writing - review & editing. **E. Xifre-Perez:** Conceptualization, Methodology, Validation, Writing - review & editing. **M.A. Tabrizi:** Conceptualization, Validation, Investigation. **J. Ferre-Borrull:** Formal analysis, Data curation. **L.F. Marsal:** Validation, Resources, Supervision, Project administration, Funding acquisition.

Acknowledgments

This work was supported in part by the Spanish Ministerio de Ciencia, Innovación y Universidades (MICINN/FEDER) RTI2018-094040-B-I00, by the Agency for Management of University and Research Grants (AGAUR) 2017-SGR-1527 and by the Catalan Institution for Research and Advanced Studies (ICREA) under the ICREA Academia Award. This project has received funding from the European Union's Horizon 2020 research and innovation program under the Marie Sklodowska-Curie grant agreement No. 713679 and from the Universitat Rovira I Virgili (URV).

References

[1] R. Jin, C. Zeng, M. Zhou, Y. Chen, Atomically Precise Colloidal Metal Nanoclusters and Nanoparticles: Fundamentals and Opportunities, Chem. Rev. 116 (2016) 10346.

[2] V. S. Guruprasad, V. Maheshwari, Magnetic nano-nets for capture of microbes in solution based on physical contact, J. Colloid Interface Sci. 535 (2019) 33.

[3] M. Zhang, W. Wang, F. Wu, P. Yuan, C. Chi, N. Zhou, Magnetic and fluorescent carbon nanotubes for dual modal imaging and photothermal and chemo-therapy of cancer cells in living mice, Carbon N. Y. 123 (2017) 70.

[4] V. P. Torchilin, Multifunctional, stimuli-sensitive nanoparticulate systems for drug delivery, Nat. Rev. Drug Discov. 13 (2014) 813.

[5] A. N. Morozovska, E. A. Eliseev, Y. M. Fomichov, Y. M. Vysochanskii, V. Y. Reshetnyak, D. R. Evans, Controlling the domain structure of ferroelectric nanoparticles using tunable shells, Acta Mater. 183 (2020) 36.

[6] I. A. Kinloch, J. Suhr, J. Lou, R. J. Young, P. M. Ajayan, Composites with carbon nanotubes and graphene: An outlook, Science 362 (2018).

[7] J. Xu, Z. Cao, Y. Zhang, Z. Yuan, Z. Lou, X. Xu, X. Wang, A review of functionalized carbon nanotubes and graphene for heavy metal adsorption from water: Preparation, application, and mechanism, Chemosphere 195 (2018) 351.

[8] H. Sun, Y. Gao, N. Hu, Y. Zhang, C. Guo, G. Gao, Z. Ma, K. I. Ivanovich, Y. Qiu, Electronic coupling between molybdenum disulfide and gold nanoparticles to enhance the peroxidase activity for the colorimetric immunoassays of hydrogen peroxide and cancer cells, J. Colloid Interface Sci. 578 (2020) 366.

[9] G. Lazzara, G. Cavallaro, A. Panchal, R. Fakhrullin, A. Stavitskaya, V. Vinokurov, Y. Lvov, An assembly of organic-inorganic composites using halloysite clay nanotubes, Curr. Opin. Colloid Interface Sci. 35 (2018) 42.

[10] Y. Wan, P. Liu, Z. Yang, S. R. Raman, G. Xiong, H. Luo, Scalable synthesis of three-dimensional interconnected mesoporous TiO2 nanotubes with ultra-large surface area, Acta Mater. 93 (2015) 138.

[11] D. Hill, A. R. Barron, S. Alexander, Comparison of hydrophobicity and durability of functionalized aluminum oxide nanoparticle coating with magnetite nanoparticles-links between morphology and wettability, J. Colloid Interface Sci. 555 (2019) 323.

[12] N. Bertrand, J. Wu, X. Xu, N. Kamaly, O. C. Farokhzad, Cancer nanotechnology: The impact of passive and active targeting in the era of modern cancer biology, Adv. Drug Deliv. Rev. 66 (2014) 2.

[13] A. Baeza, M. Colilla, M. Vallet-Regí, Advances in mesoporous silica nanoparticles for targeted stimuli-responsive drug delivery, Expert Opin. Drug Deliv. 12 (2015) 319.

[14] E. A. Sykes, J. Chen, G. Zheng, W. C. W. Chan, Investigating the impact of nanoparticle size on active and passive tumor targeting efficiency, ACS Nano 8 (2014) 5696

[15] V. M. Andrade, R. J. Caraballo Vivas, S. S. Pedro, J. C. G. Tedesco, A. L. Rossi, A. A. Coelho, D. L. Rocco, M. S. Reis, Magnetic and magnetocaloric properties of La0.6Ca0.4MnO3 tunable by particle size and dimensionality, Acta Mater. 102 (2016) 49.

[16] W. Lu, J. Li, Y. Sheng, X. Zhang, J. You, L. Chen, One-pot synthesis of magnetic iron oxide nanoparticle-multiwalled carbon nanotube composites for enhanced removal of Cr(VI) from aqueous solution, J. Colloid Interface Sci. 505 (2017) 1134.

[17] X. Wan, Y. Zhan, Z. Long, G. Zeng, Y. He, Core@double-shell structured magnetic halloysite nanotube nano-hybrid as efficient recyclable adsorbent for methylene blue removal, Chem. Eng. J. 330 (2017) 491.

[18] Y. He, S. Yang, H. Liu, Q. Shao, Q. Chen, L. Chang, J. Yuanli, L. Chuntai, G. Zhanhu, Reinforced carbon fiber laminates with oriented carbon nanotube epoxy nanocomposites: Magnetic field assisted alignment and cryogenic temperature mechanical properties, J. Colloid Interface Sci. 517 (2018) 40.

[19] M. M. Lu, M. S. Cao, Y. H. Chen, W. Q. Cao, J. Liu, H. L. Shi, D. Q. Zhang, W. Z. Wang, J. Yuan, Multiscale Assembly of Grape-Like Ferroferric Oxide and Carbon Nanotubes: A Smart

Absorber Prototype Varying Temperature to Tune Intensities, ACS Appl. Mater. Interfaces 7 (2015) 19408.

[20] A. Fernández-Pacheco, R. Streubel, O. Fruchart, R. Hertel, P. Fischer, R. P. Cowburn, Three-dimensional nanomagnetism, Nat. Commun. 8 (2017) 15756.

[21] W. Hu, G. Z. Lum, M. Mastrangeli, M. Sitti, Small-scale soft-bodied robot with multimodal locomotion, Nature 554 (2018) 81.

[22] H. Masuda, H. Yamada, M. Satoh, H. Asoh, M. Nakao, T. Tamamura, Highly ordered nanochannel-array architecture in anodic alumina, Appl. Phys. Lett. 71 (1997) 2770.

[23] A. Santos, L. Vojkuvka, J. Pallarés, J. Ferré-Borrull, L. F. Marsal, In situ electrochemical dissolution of the oxide barrier layer of porous anodic alumina fabricated by hard anodization, J. Electroanal. Chem. 632 (2009) 139.

[24] C. Eckstein, L. K. Acosta, L. Pol, E. Xifre-Perez, J. Pallares, J. Ferre-Borrull, L. F. Marsal, Nanoporous Anodic Alumina Surface Modification by Electrostatic, Covalent, and Immune Complexation Binding Investigated by Capillary Filling, ACS Appl. Mater. Interfaces 10 (2018) 10571.

[25] A. Santos, V. S. Balderrama, M. Alba, P. Formentin, J. Ferre-Borrull, J. Pallares, L. F. Marsal, Nanoporous anodic alumina barcodes: Toward smart optical biosensors, Adv. Mater. 24 (2012) 1050.

[26] L. K. Acosta, F. Bertó-Roselló, E. Xifre-Perez, A. Santos, J. Ferré-Borrull, L. F. Marsal, Stacked Nanoporous Anodic Alumina Gradient-Index Filters with Tunable Multispectral Photonic Stopbands as Sensing Platforms, ACS Appl. Mater. Interfaces 11 (2019) 3360.

[27] A. Santos, J. Ferré-Borrull, J. Pallarès, L. F. Marsal, Hierarchical nanoporous anodic alumina templates by assymetric two-step anodization, Phys. Status Solidi Appl. Mater. Sci. 208 (2011) 668.

[28] A. Santos, L. Vojkuvka, Maria Alba, V. S. Balderrama, J. Ferre-Borrull, J. Pallares, L. F. Marsal, Understanding and morphology control of pore modulations in nanoporous anodic alumina by discontinous anodization, Phys. Status Solidi Appl. Mater. Sci. 209 (2012) 2045.

[29] L. Yi, L. Zhiyuan, H. Xing, L. Yisen, C. Yi, Investigation of intrinsic mechanisms of aluminium anodization processes by analyzing the current density, RSC Adv. 2 (2012) 5164

[30] W. Lee, K. Schwirn, M. Steinhart, E. Pippel, R. Scholz, U. Gösele, Structural engineering of nanoporous anodic aluminium oxide by pulse anodization of aluminium, Nat. Nanotechnol. 3 (2008) 234.

[31] Y. Wang, A. Santos, A. Evdokiou, D. Losic, Rational design of ultra-short anodic alumina nanotubes by short-time pulse anodization, Electrochim. Acta 154 (2015) 379.

[32] Y. Wang, A. Santos, G. Kaur, A. Evdokiou, D. Losic, Structurally engineered anodic alumina nanotubes as nano-carriers for delivery of anticancer therapeutics, Biomaterials 35 (2014) 5517.

[33] Y. Wang, G. Kaur, A. Zysk, V Liapis, S. Hay, A. Santos, D. Losic, A. Evdokiou, Systematic invitro nanotoxicity study on anodic alumina nanotubes with engineered aspect ratio: Understanding nanotoxicity by a nanomaterial model, Biomaterials 46 (2015) 117.

[34] S. Bhattacharjee, DLS and zeta potential - What they are and what they are not?, J. Control. Release 235 (2016) 337.

[35] Y. Joo, Y. Jeon, S. U. Lee, J. H. Sim, J. Ryu, S. Lee, H. Lee, D. Sohn, Aggregation and stabilization of carboxylic acid functionalized halloysite nanotubes (HNT-COOH), J. Phys. Chem. C 116 (2012) 18230.

[36] M. Zhu, L. Liu, Z. Wang, Mesoporous silica via self-assembly of nano zinc amino-tris-(methylenephosphonate) exhibiting reduced fire hazards and improved impact toughness in epoxy resin, J. Hazard. Mater. 392 (2020) 122343.

[37] M. Karimi, A. Ghasemi, P. S. Zangabad, R. Rahighi, S. M. Moosavi Basri, H. Mirshekari, M. Amiri, Z. Shafaei Pishabad, A. Aslani, M. Bozorgomid, D. Ghosh, A. Beyzavi, A. Vaseghi, A. R. Aref, L. Haghani, S. Bahrami, M. R. Hamblin, Smart micro/nanopartiles in stimulus-responsive drug/gene delivery systems, Royal Society of Chemistry 45 (2016) 1457.

[38] N. Song and Y. W. Yang, Molecular and supramolecular switches on mesoporous silica nanoparticles, Chem. Soc. Rev. 44 (2015) 3474.

[39] V. Georgakilas, J. N. Tiwari, K. C. Kemp, J. A. Perman, A. B. Bourlinos, K. S. Kim, R. Zboril, Noncovalent Functionalization of Graphene and Graphene Oxide for Energy Materials, Biosensing, Catalytic, and Biomedical Applications, Chem. Rev. 116 (2016) 5464.

[40] M. Hiraoui, M. Guendouz, N. Lorrain, A. Moadhen, L. Haji, M. Oueslati, Spectroscopy studies of functionalized oxidized porous silicon surface for biosensing applications, Mater. Chem. Phys. 128 (2011) 151.

[41] M. Amouzadeh Tabrizi, J. Ferré-Borrull, L. F. Marsal, Highly sensitive IRS based biosensor for the determination of cytochrome c as a cancer marker by using nanoporous anodic alumina modified with trypsin, Biosens. Bioelectron. 149 (2020) 111828.

[42] R. Edelman, Y. G. Assaraf, I. Levitzky, T. Shahar, Y. D. Livney, Hyaluronic acid-serum albumin conjugate-based nanoparticles for targeted cancer therapy, Oncotarget 8 (2017) 24337.

[43] G. C. Wood, A Model for the Incorporation of Electrolyte Species into Anodic Alumina, J. Electrochem. Soc. 143 (2006) 74.

[44] J. T. Domagalski, E. Xifre-Perez, A. Santos, J. Ferre-Borrull, and L. F. Marsal, Tailor-engineered structural and physico-chemical properties of anodic alumina nanotubes by pulse anodization: A step forward, Microporous Mesoporous Mater. 303 (2020) 110264.

[45] R. Ozao, H. Yoshida, T. Inada, M. Ochiai, Sulfur concentration in nanoporous alumina membrane. Studied by TA and XPS, J. Therm. Anal. Calorim. 72 (2003) 113.

[46] E. Vidak, U. Javoršek, M. Vizovišek, B. Turk, Cysteine Cathepsins and their Extracellular Roles: Shaping the Microenvironment, Cells 8 (2019) 264.

[47] X. F. Zhao, J. X. Wang, F. X. Li, S. Sueda, H. Kondo, Analysis of substrate specificity and endopeptidyl activities of the cathepsin B-like proteinase from Helicoverpa armigera, Protein J. 24 (2005) 219.

[48] L. Z. Swisher, A. M. Prior, S. Shishido, T. A. Nguyen, D. H. Hua, J. Li, Quantitative electrochemical detection of cathepsin B activity in complex tissue lysates using enhanced AC voltammetry at carbon nanofiber nanoelectrode arrays, Biosens. Bioelectron. 56 (2014) 129.

[49] Y. Song, H. Fan, M . J. Anderson, J. G. Wright, D. H. Hua, J. Koehne, M. Meyyappan, J. Li, Electrochemical activity assay for protease analysis using carbon nanofiber nanoelectrode arrays, Anal. Chem. 91 (2019) 3971.

[50] G. Hungerford, J. Benesch, J. F. Mano, R. L. Reis, Effect of the labelling ratio on the photophysics of fluorescein isothiocyanate (FITC) conjugated to bovine serum albumin,

Photochem. Phtobiol. Sci. 6 (2007) 152.

[51] Y. Wang, I. Zinonos, A. Zysk, V. Panagopoulos, G. Kaur, A. Santos, D. Losic, A. Evdokiou, In vivo toxicological assessment of electrochemically engineered anodic alumina nanotubes: a study of biodistribution, subcutaneous implantation and intravenous injection, J. Mater. Chem. B 5 (2017) 2511.

[52] M. Fizir, P. Dramou, K. Zhang, C. Sun, C. Pham-Huy, Polymer grafted-magnetic halloysite nanotube for controlled and sustained release of cationic drug, J. Colloid Interface Sci. 505 (2017) 476.

[53] M. A. Tabrizi, J. Ferré-Borrull, L. F. Marsal, An optical biosensor for the determination of cathepsin B as a cancer-associated enzyme using nanoporous anodic alumina modified with human serum albumin-thionine, Microchim. Acta 187 (2020) 230.